Innovative formulation for topological fatigue optimisation based on material defects distribution and TopFat algorithm

Original
Innovative formulation for topological fatigue optimisation based on material defects distribution and TopFat algorithm / Gao, X., Caivano, R., Tridello, A., Chiandussi, G., Ma, H., Paolino, D., Berto, F.. - In: INTERNATIONAL JOURNAL OF FATIGUE. - ISSN 0142-1123. - STAMPA. - 147:(2021), p. 106176. [10.1016/j.ijfatigue.2021.106176]

Publisher:
Elsevier

Published
DOI:10.1016/j.ijfatigue.2021.106176

Innovative formulation for topological fatigue optimisation based on material defects distribution and TopFat algorithm

Xingjun Gao[1], Riccardo Caivano[2,*], Andrea Tridello[2], Giorgio Chiandussi[2], Haitao Ma[3], Davide Paolino[2], Filippo Berto[4]

[1] *School of Civil and Transportation Engineering, Guangdong University of Technology, Guangzhou, 510006, PR China*

[2] *Department of Mechanical and Aerospace Engineering, Politecnico di Torino, 10129 Turin, Italy*
[*] Corresponding author, riccardo.caivano@polito.it

[3] *Earthquake Engineering Research and Test Centre, Guangzhou University, Guangzhou, 510405, PR China*

[4] *Department of Mechanical and Industrial Engineering, Norwegian University of Science and Technology (NTNU), Trondheim, Norway*

Abstract

In the present study, a novel defect-driven topological fatigue (TopFat) optimisation approach is proposed. The influence of defects on the fatigue strength is modelled by using the Murakami formulation to consider the defect distribution in the material. The fatigue strength is taken into consideration by introducing a stress constraint in the minimum compliance topology optimisation problem in addition to the von Mises stress and volume constraints. The algorithm has been effectively validated on several literature cases, providing optimized topologies with maximised stiffness under the prescribed quasi-static and fatigue strength requirements.

Keywords: Topology optimisation; Fatigue; Stress constraint; Defect population; Murakami fatigue limit

1. Introduction

In the last decades, metal additive manufacturing (AM) technologies together with topology optimisation (TO) have revolutionized the design and the production of mechanical components. Indeed, AM processes allow the production of complex geometries [1–4] with fewer manufacturing constraints compared to traditional processes as reported by [5] ("The additive method is unlike traditional mass production manufacturing methods in many ways, creating new possibilities for designers to realise new and different design ideas previously impossible to manufacture.") As an example, the complex optimised geometries by TO [6,7] or the lattice structures [8] can be manufactured with AM technologies, while they would be almost unproducible with traditional technologies such as drilling, milling or turning. Therefore, this enhanced manufacturing freedom can be hardly fully exploited with the traditional design methodologies. On the contrary, TO provides an ideal tool for the design of optimized components [6,9–12] to be produced with AM processes. TO basically permits to find the ideal material distribution to optimize one or more properties (e.g., stiffness) under various constraints [13]. Many approaches have been developed for solving the TO problem (see [14] and references there in). Commonly, the objective of TO is to maximise the stiffness of the structure under a volume constraint. However, in this case the maximum allowable stress in the structure is not considered and the optimized topology can hardly be used since it probably does not meet the safety requirements. For this reason, limits on the allowable stress, depending on the application, must be included in the TO problem formulation. Generally, when a component is designed with a TO algorithm, the stress is limited by considering the quasi-static material strength (i.e. von Mises stress [15] or buckling stress [16]). More recently, algorithms also capable to consider the fatigue strength have been proposed [13-24]. For example, in [17] a fatigue driven TO algorithm where the fatigue constraint is substituted by multiple stress constraints according to traditional high-cycle fatigue design methodology [29] is proposed. Similarly, in [18] the equivalent static stress approach has been employed for the high-cycle fatigue stress assessment considering the Sines method and a modified Goodman criterion. In [27] the dynamic fatigue failure constraints according to Crossland's criterion are included. In [19] a TO algorithm for finite-life high-cycle fatigue damage using a density approach and analytical gradients is proposed. In [26] random fatigue loads are analysed with different methodologies, such as narrow-band solution, the Wirsching and Light method, the Ortiz and Chen method, and the Dirlik method and taken into account in structural TO.

It is therefore clear, according to the literature results, that the research of TO algorithms capable of considering the fatigue constraints is of utmost interest.

However, the fatigue limit inserted as a constraint in TO algorithms is generally extrapolated by classical fatigue theory (e.g., the asymptote at the end of the S-N curve for steel materials), which is surely effective for a large of real applications but can miss the crucial influence of defects inside the material. Indeed, it is well-known that in many practical applications and in-service conditions, the fatigue response of components is controlled by defects (e.g., inclusions, porosity) which form during the manufacturing process. In this case, the fatigue strength is smaller than the fatigue strength of a component free of defects, according to [30]. Therefore, the TO algorithm as a design tool must include this defect-driven constrain for the fatigue response in order to avoid premature failures in the optimised components. For example, it is well-known that the fatigue response of AM parts is critical and the main reason is the presence of large defects that originates during the production process [31–35]. The influence of defects therefore cannot be neglected to ensure a safe and appropriate design. It must be considered when the component is designed through TO algorithms, thus permitting to define the topology which ensures the best material exploitation while guaranteeing the structural safety.

To the authors' knowledge, the influence of defects on the (lowered) fatigue response has not been included in the TO yet. Interestingly, in [36] the influence of porosity on structural safety is included in the

TO algorithm. However, the parameters related to the porosity size and shape of the holes are not fitted with experimental data and a direct link with the fatigue response of the optimised part is missing. Moreover, the defect size is a priori or randomly assumed and the dependence between the defect size and the material volume is not considered. Moreover, an arbitrary choice of the defect size could not be effective, since the defect size and its influence on the fatigue response depend on many factors (e.g., the material microstructure) and must be properly assessed for each material. In the present paper, a new TO formulation and corresponding solution algorithm is proposed (TopFat) for considering the influence of defects on the fatigue response. The fatigue limit of the component is assessed by considering the Murakami formulation [30]. In order to take into account, the presence of defects with different morphologies and chemical composition, an equivalent defect size is considered, according to [30]. In order to model the dependence between the defect size and the material volume, the distribution of defects size is assumed to follow the Largest Extreme Values Distribution (LEVD). Indeed, according to [30], the largest defect within the material controls the fatigue response. Therefore, the size of the largest defect, rather than the defect density, controls the fatigue response. For example, the fatigue response of a component with a large number of small defects (higher defect density) is larger than that the fatigue response of a part with a small number of defects, but with larger size. This experimental evidence [30,37] justifies the use of the LEVD for the estimation of the defect size [37]. All the information about the Murakami theory and its application in the TopFat algorithm is detailed in the following section. The analytical formulation of the proposed algorithm is firstly defined, by considering concurrently quasi-static and fatigue stress constraints, when the component is subjected to load cycles with minimum stress equal to 0 (i.e., stress ratio equal to 0). The proposed algorithm is finally validated with literature benchmarks, proving its effectiveness and the importance of considering the presence of defects to guarantee the overall structural integrity of the part.

The rest of this paper is organized as follows: in **Section 2** the fatigue model in presence of defects is described; in **Section 3** the TO problem and its solution are reported; in **Section 4** the test cases employed for the validation of the proposed algorithm are illustrated. Concluding remarks are finally made in **Section 5**. The hybrid stress element model employed for the test cases in detailed in **Appendix A.** The sensitivity analysis is provided in **Appendix B**.

2. Fatigue response in the presence of defects

The influence of small defects on the fatigue response of components has been widely investigated in the literature and the well-known Murakami formulation [30] is generally considered to assess the fatigue strength, $\bar{\sigma}^f$, in presence of defects:

$$\bar{\sigma}^{f} = \frac{C_1 \cdot (HV + 120)}{(\sqrt{a})^{\frac{1}{6}}} \cdot \left(\frac{1-R}{2}\right)^{0.226 + HV \cdot 10^{-4}} \tag{1}$$

where C_1 is a constant parameter depending on the defect location, HV is the Vickers hardness of the material accounting for the influence of the microstructure, $\sqrt{a}$ is the square root of the area of the defect measured in a plane perpendicular to the maximum applied stress and R is the stress ratio From a physical point of view, Eq. (1) states that the fatigue strength of the material in presence of defects depends on the material hardness, correlated to the microstructure, on the defect size and on the stress ratio. In particular, an increment of the Vickers hardness has a positive effect on the fatigue strength. On the other hand, the larger the defect size, the smaller the fatigue strength. Since different defects (i.e., with different chemical composition and morphology) could form during the manufacturing processes, especially for AM processes, an equivalent defect size can be considered for $\sqrt{a}$, according to [30]. Moreover, for $\sqrt{a}$, positive stress ratios R lower the fatigue response. According to [30], Eq. (1) is obtained by equating the Stress Intensity Factor (SIF) associated with the defect to the SIF threshold of the material and permits to assess the stress amplitude below which a crack does not propagate from a defect with size equal to $\sqrt{a}$. Accordingly, in order to prevent fatigue failures originating from defects, the most critical defect in the component volume should be reliably known. The critical defect corresponds the largest defect present in the material: according to Eq. (1), the larger the defect size, the smaller the fatigue limit. Therefore, the largest defect is the "critical defect". It is clear that the size of the critical defect is not known when a component is designed, since the defect population depends on a large bulk of different factors and mainly on the manufacturing processes. For example, for parts produced through AM processes [31–35], the process parameters strongly affect the defect population.

In order to clarify this aspect, Fig. 1 shows the steps that are generally followed for the design of components with topology optimisation algorithms (e.g., AM parts). After setting the design domain and the optimisation parameters, the TO algorithm provides the topology that minimizes the compliance under the volume constraint. The component is finally manufactured and, depending on the manufacturing process, it may contain manufacturing defects, highlighted in Fig. 1 with yellow circles, which significantly affect the fatigue response. Material defects can be detected with non-destructive techniques: however, the assessment of the defect population once the component has been manufactured prevents any possible modification.

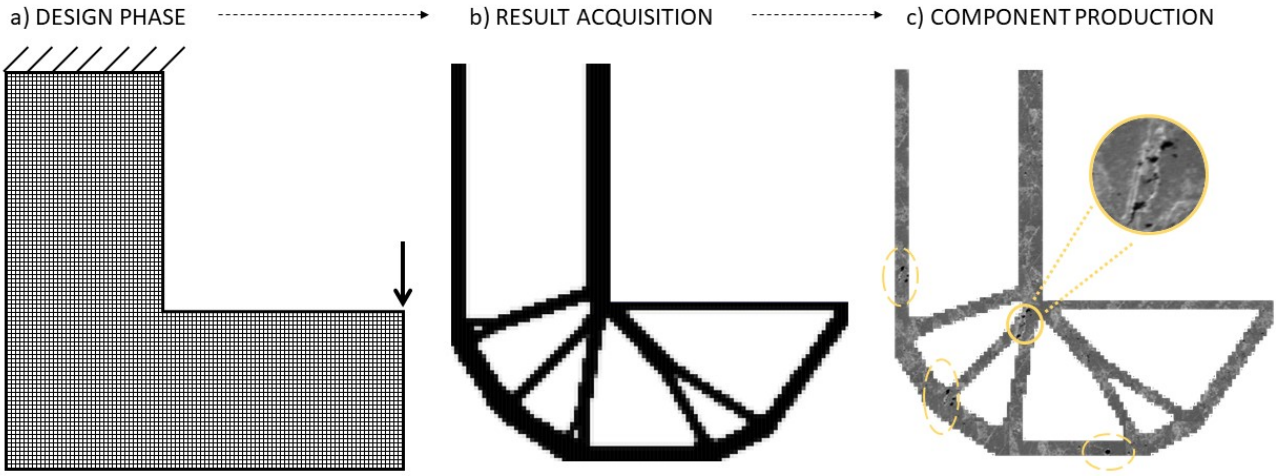

Figure 1 – Qualitative component flow from the initial design domain to the realisation. a) The optimisation process is set out, b) the algorithm provides the minimum compliance topology under volume constraint, c) the component is realised, and the material presents a defect distribution.

Therefore, for a proper fatigue design, the possible presence of defects must be taken into consideration when the component is designed. In particular, the defect size distribution in the material and, accordingly, the critical defect size (i.e., the size of the largest defect within the material volume) must be reliably assessed. According to the literature, the defect size is a random variable and is assumed to follow the Largest Extreme Value Distribution (LEVD). The related Cumulative Distribution Function (CDF), $P_{\sqrt{a}}$, of the LEVD is given as follows:

$$P_{\sqrt{a}}(\sqrt{a}) = e^{-e^{-\left(\frac{\sqrt{a}-\mu_{\sqrt{a}}}{\sigma_{\sqrt{a}}}\right)}} \tag{2}$$

where $\mu_{\sqrt{a}}$ and $\sigma_{\sqrt{a}}$ are the location and the scale parameters of the distribution, respectively. From a physical point of view, Eq. (2) permits to compute the probability $P_{\sqrt{a}}$ of having a defect with size smaller than $\sqrt{a}$. The parameters $\mu_{\sqrt{a}}$ and $\sigma_{\sqrt{a}}$, that depends on the material, the production process and on possible post treatment, can be estimated experimentally by assessing the largest defect within samples with a defined volume V_0 (reference volume in the following). Different methodologies are employed in the literature for the parameter estimation, like defect sampling on polished metallurgical samples or by considering the defect originating the fatigue failure in fatigue tests. According to the properties of the LEVD, Eq. (2) can be also rewritten to predict the size of the largest defect in a volume V_n n times V_0. Indeed, the defect size is dependent on the material volume, i.e., the larger the volume, the larger the probability of defects with larger size. Therefore, the parameters $\mu_{\sqrt{a}}$ and $\sigma_{\sqrt{a}}$ estimated for a material volume equal to V_0, can be used to predict the size of the largest defect within a larger volume V_n, by exploiting the properties of the LEVD distribution. The largest defect size, $\sqrt{a}_n$, in a material volume n times V_0 can be obtained through Eq. (3) by shifting the original distribution in Eq. (2); for more details on the LEVD and on its properties for the assessment of the defects in the material, the reader can refer to [30].

$$\sqrt{a}_n = \mu_{\sqrt{a}} + \sigma_{\sqrt{a}} \cdot (-\,ln(-\,ln(P)) + ln(n)) \tag{3}$$

Eq. (3) permits to assess the probability of a defect wit size $\sqrt{a}_n$ in a volume V_n or to assess the P percentile of the defect size in the volume V_n.

Therefore, estimated the constant coefficients $\mu_{\sqrt{a}}$ and $\sigma_{\sqrt{a}}$ and for a probability P, the fatigue strength in the component volume V_n can be reliably predicted by combining Eq. (1) and Eq. (3):

$$\bar{\sigma}^f = \frac{C_1 \cdot (HV + 120)}{\left(\mu_{\sqrt{a}} + \sigma_{\sqrt{a}} \cdot \left(-\,ln(-\,ln(P)) + ln\left(\frac{V_n}{V_0}\right)\right)\right)^{\frac{1}{6}}} \cdot \left(\frac{1-R}{2}\right)^{0.226 + HV \cdot 10^{-4}} \tag{4}$$

Eq. (3) can therefore be used for assessing the fatigue strength in a volume where defects are present and could originate the fatigue cracks. The fatigue strength in Eq. (4) can be used as stress limit when components are to be designed. In the proposed methodology, Eq. (4) is implemented in a TO algorithm in order to consider the influence of defects on the fatigue response.

3. Topology optimisation in presence of defects: analytical formulation

In this section the analytical formulation of the TO algorithm is provided. In Section 3.1, the optimisation function and the constraints are defined, whereas in Section 3.2 the numerical implementation is described. Finally, in Section 3.3 the solution algorithm is outlined.

3.1 Optimisation function

The finite element method (FEM) is employed for the optimisation. The design domain is discretized by finite elements and the final material distribution is achieved by varying the density of each element, according to the SIMP (Solid Isotropic Material with Penalization) interpolation model [13,38]. The density of the e^{th} element, ρ_e, is in the range $[0,1]$. Therefore, the final material distribution corresponds to the set of elements where the density is equal to 1. On the contrary, those elements with null density are considered as void material. During the optimisation process element densities can assume intermediate values between 0 and 1 describing the so-called ‘grey’ zones. However, the final topology must be described only by black and white zones, i.e. a clear distribution of full and void material. Following the SIMP approach, the relationship between the variable density and the mechanical properties of the element is given by:

$$\boldsymbol{K}_e = \rho_e^p \boldsymbol{K}_0 \tag{5}$$

where $\boldsymbol{K}_e$ is the stiffness matrix of the e^{th} element, $\boldsymbol{K}_0$ is the stiffness matrix of the element with solid material and $p \geq 1$ is the penalty factor. The exponent p is usually set equal to 3 and is used in the SIMP method to force the element density to either 0 or 1 at the end of the optimisation process, since elements with intermediate density have no physical meaning. Indeed, the power function penalizes the intermediate density, forcing the solution to converge to the desired binary distribution.

Eq. (6) shows the proposed TO formulation, which involves the minimization of the component compliance with defined volume and stress constraints (i.e., von Mises and first principal alternate stress):

$$
\begin{aligned}
&\text{find } \boldsymbol{\rho} = \{\rho_1, \rho_2, \dots, \rho_{N_e}\} \\
&\min\ C = \boldsymbol{F}^T \boldsymbol{U}(\boldsymbol{\rho}) = \boldsymbol{U}(\boldsymbol{\rho})^T \boldsymbol{K}(\boldsymbol{\rho}) \boldsymbol{U}(\boldsymbol{\rho}) \\
&\text{s.t.} \begin{cases}
\boldsymbol{K}(\boldsymbol{\rho}) \boldsymbol{U}(\boldsymbol{\rho}) = \boldsymbol{F} \\
V(\boldsymbol{\rho}) \leq \bar{V} \\
\sigma_e^{\mathrm{vM}}(\boldsymbol{\rho}) \leq \bar{\sigma}^s \quad e = 1,2,\cdots,N_e \\
\sigma_e^1(\boldsymbol{\rho}) \leq \bar{\sigma}^f \quad if\ \hat{\sigma}_e^1(\boldsymbol{\rho}) > 0 \quad e = 1,2,\cdots,N_e \\
\underline{\rho} \leq \rho_e \leq 1 \quad e = 1,2,\cdots,N_e
\end{cases}
\end{aligned}
\tag{6}
$$

where $\boldsymbol{\rho} = \rho_e\ (e = 1,2,\dots,N_e)$ are the design variables, i.e. the densities. N_e is the total number of elements, C is the global compliance, $\boldsymbol{F}$ is the vector of the global forces, $\boldsymbol{U}$ is the vector of the global displacements, $\boldsymbol{K}$ is the global stiffness matrix, V is the volume of the component, $\bar{V}$ is the upper volume limit, σ_e^{vM} is the von Mises stress for the e^th^ element, $\bar{\sigma}^s$ is the von Mises upper bound, σ_e^1 is the first principal alternate stress for the eth element, $\bar{\sigma}^f$ is the upper limit of the first principal alternate stress defined in Eq. (4), $\hat{\sigma}_e^1$ is the first principal stress for the eth element and $\underline{\rho}$ is the minimum density of the element. The complete expressions of σ_e^{vM}, σ_e^1 and $\hat{\sigma}_e^1$ are reported in Section 3.2 in Eq. (7) – (11) and properly described. The parameter $\underline{\rho}$ is usually set in TO problems in the range $[0.0001{,}0.001]$, in order to avoid singularities in the global stiffness matrix [38].

The solution that minimizes the compliance under the volume constraint and no other stress or fatigue constraint, provides the optimized material distribution, but stress peaks are likely and are not controlled. This would be detrimental for the structural integrity of the optimized topology and would prevent the use of the TO algorithm for components. For this reason, the stress constraints are included in the formulation. In particular, the formulation defined in Eq. (6) permits to assess the optimized topology for a component subjected to a cyclic force in the range $[0, F_{max}]$, F_{max} being the maximum applied force in the load cycle, corresponding to a stress ratio R equal to 0. In order to prevent failures from defects that are randomly distributed within the material volume, the first principal alternate stress in each element is limited by the first principal alternate stress upper limit, $\bar{\sigma}^f$, corresponding to the fatigue strength defined in Eq. (4). Indeed, the first principal alternate stress is responsible for the crack propagation from defects. However, the first principal alternate stress is always a positive term but it must be limited only in the elements with a positive first principal stress (i.e., $if\ \hat{\sigma}_e^1(\boldsymbol{\rho}) > 0$ in Eq. (6)), since only positive first principal stresses permit the crack propagation up to failure. For the sake of clarity, only positive $\hat{\sigma}_e^1$ permits the crack propagation, if a defect is present. On the other hand, if the element is subjected to a compression stress, the crack will not propagate, according to [29,30]. As the volume constraint will be active, the fatigue limit is computed by considering $V_n = \bar{V}$. Accordingly, it is conservatively assumed that a defect with the same size of a defect that can be statistically found in a volume corresponding to $\bar{V}$ is present in each element In other words, the fatigue stress constraint is applied to each element, as if the largest defect is found in each element. This assumption is rather conservative, but it permits a rapid convergence of the method (see Section 3.2 and Section 4). On the other hand, it is worth to note that the fatigue crack does not propagate in regions of material subjected to a compression state during the load cycle. However, if a stress limit is not considered for elements in compression, the optimized component could fail due to possible peak stresses in these elements (e.g., the stress in the element could be larger than the quasi-static strength of the material). For this reason, a second stress constraint is introduced to ensure that the von Mises stress for each element is below an admissible stress (e.g., the yield strength divided by an appropriate safety factor). This second stress constraint is verified for each element: it is worth to note that, for elements subjected to a positive first principal stress and therefore at risk of crack propagation in presence of defects, the most restrictive stress constraint prevails in the optimisation process. This simplifies the numerical implementation of the proposed methodology

3.2 Numerical implementation

In this Subsection, the numerical details employed to guarantee valid TO results are presented. In Subsection 3.2.1, a brief description of the employed hybrid stress element model is provided. In Subsection 3.2.2, the relaxation method, the stress aggregation function and the STM-based correction scheme used to provide stress constraint esteem are detailed. Finally, in Subsection 3.2.3 the continuation, filtering and projection techniques considered to obtain clear black-and-white domain and avoid local minima are described.

3.2.1 Hybrid stress element model

The proposed methodology has been numerically implemented for bidimensional cases. In the literature, for bidimensional cases, density-based TO is commonly carried out using bilinear quadrilateral four-node elements. The main reason lies in the low computational cost of this element model. However, when an explicit stress evaluation is required, these elements may produce inaccurate results due to the shear locking effect, especially in bending dominated regions [39]. To overcome this issue and improve the accuracy of the results, a four-node hybrid stress element model is employed in this study. In this model, both the displacement and stress fields are approximated by means of interpolation functions. The basic idea behind this method is to make the element less sensitive to geometrical distortions and improve therefore the stress accuracy evaluation. This result can be achieved by adding additional nodes too, but this would increase remarkably the computational cost. It has been proved that this method can produce more accurate results, at the same mesh discretization, with respect to classical bilinear quadrilateral four-node elements [40].

All considered, the element stress vector $\boldsymbol{\sigma}_e$ in the hybrid stress element (Voigt notation) and the SIMP framework is given by:

$$\boldsymbol{\sigma}_e(\boldsymbol{\rho},\xi,\eta) = [\sigma_{ex} \quad \sigma_{ey} \quad \tau_{exy}]^T = \rho_e^{\gamma}\boldsymbol{\Phi}(\xi,\eta)\boldsymbol{\beta}_e \tag{7}$$

where σ_{ex}, σ_{ey} and τ_{exy} are the element stress components, γ is a scalar parameter which value depends on the type of stress interpolation employed (detailed in the following section), $\boldsymbol{\Phi}(\xi,\eta)$ is the geometrical interpolation matrix depending on the element natural coordinates ξ and η, $\boldsymbol{\beta}_e$ is the stress parameter vector. The first term modifies the stress according to the local density dictated by the TO approach. The second term defines where the stress is evaluated within the element according to the natural coordinates ξ and η. The third term $\boldsymbol{\beta}_e$ relates the displacement fields with the stress considering the material elasticity, the strain-displacement matrix and the structure thickness, similarly to the classical finite element model. All the details related to the Eq. (7) and how the term $\boldsymbol{\beta}_e$ is numerically evaluated are reported in appendix A. In all the further analysis, it has been chosen to evaluate the stress element vector $\boldsymbol{\sigma}_e$ in the element centre, i.e. $\boldsymbol{\Phi}(0,0)$**,** according to [39]. In order to simplify the notation, the stress element vector evaluated in the element centre $\boldsymbol{\sigma}_e(\boldsymbol{\rho},0,0)$ is renamed as $\boldsymbol{\sigma}_{ce}(\boldsymbol{\rho})$ in the following.

3.2.2 Stress constraints: relaxation method, aggregation measure and correction scheme

When the stress constraint is considered in the TO problem formulation, some issues must be managed in order to obtain a clear convergence and a correct final topology. Firstly, the stress constraint is for its own nature a local constraint and during the optimisation it is likely to be discontinue within the domain, leading to singular optimum. This problem is so-called *stress singularity* and it belongs to the set of singularity problems in structural optimisation, well-known and widely described in the literature from many decades [41].

In this study, the stress singularity is avoided through the *qp-relaxation strategy* [42], which uses two different penalization factors for the stiffness and the stress. This strategy consists of penalizing the element stiffness in Eq. (5) with the parameter p while the stress in Eq. (7) is penalized with another exponent, q. Therefore, the discontinuity in the constraints is smoothed by relaxing the penalization applied to the stress measure. Namely, the predefined parameter γ in Eq. (7) is equal to q, whose value has been set equal to 0.5 as done in [39]. Some other relaxation approaches are also available in the literature: e.g., the *ε-relaxation* method [43] or the *stress penalization* method [44]. However, it has been decided to employ the *qp-relaxation strategy* since it has been found to be one of the most effective and straightforward technique to solve the stress singularity [39].

Given the element stress vector properly penalised and evaluated in the element centre $\boldsymbol{\sigma}_{ce}(\boldsymbol{\rho})$, it is possible to calculate the von Mises and first principal alternate stress. In particular, the von Mises stress for the e^{th} element can be evaluated as follows:

$$\sigma_e^{\mathrm{vM}}(\boldsymbol{\rho}) = (\boldsymbol{\sigma}_{ce}^T \boldsymbol{V} \boldsymbol{\sigma}_{ce})^{\frac{1}{2}} \tag{8}$$

where:

$$\boldsymbol{V} = \begin{bmatrix} 1 & -1/2 & 0 \\ -1/2 & 1 & 0 \\ 0 & 0 & 3 \end{bmatrix} \tag{9}$$

The first principal alternate stress, under the plane stress hypothesis for bidimensional structure, is, in matrix notation:

$$\sigma_{ce}^1 = \boldsymbol{\sigma}_{ce}^T \boldsymbol{V}_1 + \frac{1}{2}(\boldsymbol{\sigma}_{ce}^T \boldsymbol{V}_2 \boldsymbol{\sigma}_{ce})^{\frac{1}{2}} \tag{10}$$

where the two matrices are respectively:

$$\boldsymbol{V}_1 = \begin{bmatrix} \frac{1}{2} & \frac{1}{2} & 0 \end{bmatrix}^{\boldsymbol{T}}, \quad \boldsymbol{V}_2 = \begin{bmatrix} 1 & -1 & 0 \\ -1 & 1 & 0 \\ 0 & 0 & 4 \end{bmatrix} \tag{11}$$

In the analysed optimisation problem, where the stress ratio R is set equal to zero, the value of $\hat{\sigma}_e^1$ is simply twice the alternate stress σ_e^1. A second problem related to stress constrained TO comes into account when looking at the number of equations involved. Indeed, if the domain is discretised by a large number, n, of elements, the stress constraint must be checked for each element, leading possibly to $2n$ constraints, n for each stress constraint. In this case, aggregation functions are used to reduce the number of constraints to a single value and improve the computational efficiency of the TO. The most employed are the *P-norm* aggregation function [45] and the *Kreisselmeier-Steinhauser (KS)* aggregation function [15,46–48]. In the presented study the K-S function is employed for both the constraints on von Mises stress and the first principal alternate stress. The aggregation functions are evaluated following Eq. (12) and Eq. (13) within the domain Ω and the subdomain Ω^1 respectively. This last sub domain is defined as the portion of the domain where the elements undergo traction stress, i.e. the first principal stress is positive as already stated in Eq. (6). It can be defined analytically as $\Omega^1 = \{e \in \Omega \mid \hat{\sigma}_e^1(\boldsymbol{\rho}) \geq 0\}$.

$$\sigma^{\mathrm{vM,\,KS}} = \frac{1}{\mu_\sigma} ln\left[\sum_{e\in\Omega} exp\left(\frac{\mu_\sigma \sigma_e^{\mathrm{vM}}}{\bar{\sigma}^s}\right)\right] \tag{12}$$

$$\sigma^{1,\,\mathrm{KS}} = \frac{1}{\mu_\sigma} ln\left[\sum_{e\in\Omega^1} exp\left(\frac{\mu_\sigma \sigma_e^1}{\bar{\sigma}^f}\right)\right] \tag{13}$$

where μ_σ is the stress aggregation parameter and it controls the approximation of $\max(\sigma_e^{\mathrm{vM}})$ and $\max(\sigma_e^1)$ which are the parameters to be effectively constrained. For lower values of μ_σ, the approximation is poor and the final mismatch between the real maximum and that evaluated through the aggregation function raises. For higher values, the accuracy increases but the induced non-linearity in the problem also rises. It must be balanced properly to achieve the best compromise. A more detailed discussion about this term and the K-S aggregation function is provided in [49].

Whereas the aggregation functions solve the high number of constrain problems, they induce approximations and higher non-linearities in the TO problems. These K-S related issues can be overcome by means of the *STM (stability transformation method)-based* stress correction scheme [50]. In all non-trivial cases, the approximations induced by the K-S aggregation function overestimates the actual maximum of element stress. Therefore, two stress constraint functions, f^{vM} and f^1, are computed by scaling down the term $\sigma^{\mathrm{vM,\,KS}}$ and $\sigma^{1,\,\mathrm{KS}}$, according to the STM-based stress correction scheme which reads:

$$f^{\mathrm{vM}} = c_s^{I,\mathrm{vM}} \cdot \sigma^{\mathrm{vM,\,KS}} \leq \bar{\sigma}^s \tag{14}$$

$$f^1 = c_s^{I,1} \cdot \sigma^{1,\,\mathrm{KS}} \leq \bar{\sigma}^f \tag{15}$$

The complete expressions of the correction factors in the STM-based stress correction scheme $c_s^{I,\mathrm{vM}}$ and $c_s^{I,1}$ are reported as below:

$$c_s^{I,\mathrm{vM}} = \begin{cases} \alpha_s^{I,\mathrm{vM}} & I = 1 \\ (1-s_0)\alpha_s^{I,\mathrm{vM}} + s_0 c_s^{I-1,\mathrm{vM}} & I > 1 \end{cases} \tag{16}$$

$$c_s^{I,1} = \begin{cases} \alpha_s^{I,1} & I = 1 \\ (1-s_0)\alpha_s^{I,1} + s_0 c_s^{I-1,1} & I > 1 \end{cases} \tag{17}$$

where I is the iteration index of the topology optimization procedure, $\alpha_s^{I,\mathrm{vM}} = \frac{max(\sigma_e^{\mathrm{vM}})_I}{\sigma^{\mathrm{vM,\,KS}}}$, $\alpha_s^{I,1} = \frac{max(\sigma_e^1)_I}{\sigma^{1,\,\mathrm{KS}}}$ and $s_0 \epsilon [0,1]$ is a relaxation parameter for avoiding possible oscillations. From the whole set of possible methodologies to solve the stress constraint related issues, the *qp-relaxation* strategy, the *K-S aggregation* function, and the *STM-based correction* scheme have been selected. This choice is justified by previous studies [16,39] which proved the effectiveness of the presented solution.

3.2.3 SIMP convergence improvements: continuation, filtering and projection

It is worth noting that the SIMP approach suffers from other criticalities, as reported in [51]. The most relevant shortcomings are briefly detailed in the following. Firstly, in order to obtain a black-and-white final topology, the penalisation factor p must be sufficiently great (usually set equal to 3). However, increasing the penalization factor forces the problem to be much more non-convex and the solution is likely to fall into local minima [38,51]. To overcome this issue, the *continuation method* is typically employed, whose effectiveness has been verified in several studies [50][52]. The penalization factor p is set to 1 at the beginning of the optimisation and then slowly increased up to 3 during the process. In this way, the solution is not forced to fall into local minima in the early stage of the process. Secondly, the so-called checkerboard effect must be tackled. It consists of a final structure where the distribution is black or white, but some elements are connected only by corners, like in a checkerboard. Numerically, the structure results to be stiffer in presence of this checkerboard-like fashion due to erroneous FE modelling with low order elements. Indeed, it is a numerically induced artificial stiffness which does not simulate correctly the real structural behaviour. Checkerboard can be avoided by using higher-order elements or employing a linear filter of the density variables [53][54]. This second option is generally preferred since it does not increase the computational effort. The density variable is substituted with the value of the linear average of the element densities in its neighbourhood. The filtered density variable $\tilde{\rho}_e$ is evaluated as follows:

$$\tilde{\rho}_e = \frac{\sum_{i \in \Omega_e} w_{ei} \rho_i V_i}{\sum_{i \in \Omega_e} w_{ei} V_i} \tag{18}$$

The set of elements in the neighbourhood Ω_e is determined by a circle with radius $\hat{R}$:

$$\Omega_e = \{ i \mid \|\boldsymbol{x}_i - \boldsymbol{x}_e\| \ \leq \ \hat{R} \} \tag{19}$$

where $\boldsymbol{x}_i$ and $\boldsymbol{x}_e$ are the coordinate vectors of the element centre. The linear weight function w_{ei} is defined as:

$$w_{ei} = \hat{R} - \ \|\boldsymbol{x}_i - \boldsymbol{x}_e\| \tag{20}$$

Lastly, the use of a filter may foster the presence of 'grey' zones in the final material distribution. To avoid intermediate densities in the final topology, a *non-linear projection* is applied to the filtered density $\tilde{\rho}_e$ [55]. The non-linear projected density $\overline{\tilde{\rho}_e}$ is defined as:

$$\overline{\tilde{\rho}_e} = \frac{\tanh(\beta \rho_0) - \tanh\big(\beta(\tilde{\rho}_e - \rho_0)\big)}{\tanh(\beta \rho_0) + \tanh\big(\beta(1 - \rho_0)\big)} \tag{21}$$

where β is the projection parameter which controls the effect of the projection and ρ_0 is the threshold parameter which is generally set to 0.5. The projection erases the ‘grey’ zones, fostering the “black or white” solution (i.e., black elements corresponds to element with density equal to 1, whereas element with density equal to 0 corresponds to void elements). In the present work, the above described filtered and projected density has been employed. Moreover, the continuation method has also been applied to the parameters β and R to avoid local minima [39].

Finally, the Method of Moving Asymptotes (MMA) [56] has been adopted to numerically solve the optimisation problem. This method is a first order-programming solver and it requires the evaluation of the first derivatives: the complete sensitivity analysis is provided in Appendix B.

3.3 Solution algorithm

To check the convergence of the MMA, the following two criteria have been used:

$$\begin{gathered}\left\|\boldsymbol{\rho}^{(I)}-\boldsymbol{\rho}^{(I-1)}\right\|_{\infty} \leq \varepsilon_{\rho} \\ \frac{\left\|C^{(I)}-C^{(I-1)}\right\|}{C^{(I)}} \leq \varepsilon_{C}\end{gathered} \tag{22}$$

where I is the iteration index, and ε_C and ε_ρ are predefined tolerances [39].

The flowchart of the proposed solution algorithm *TopFat* is reported in Fig. 2, the numbers indicate the various steps of the method. It can be split into two main different phases. The first phase (1) consists of the evaluation of the defect population and related stress limit according to Murakami theory. Then the second phase (2), where the proper topology optimisation is carried out considering the defect distribution. The defect population analysis in TopFat starts with the optimisation model definition (1.1), i.e. the design domain, the application of the boundary conditions and the material model. In this step, the solution parameters are defined too. Step 1.2 consists of the defect population estimation according to LEVD, the evaluation of the size $\sqrt{a}$ of the most critical one. In step 1.3 the information about the defect population is converted in the admissible first principal alternate stress following the Murakami theory. After that, the topology optimisation phase starts, and it begins with the filtering and the projection of the density variables (2.1). Step 2.2 consists of the finite element analysis and therefore the evaluation of the compliance, the volume and the stress functions within the domain. The sensitivity of these quantities with respect to the density variables follows (2.3). The updating of the new distribution of the density variables by means of the MMA method is carried out in step 2.4. Finally, in step 2.5 the convergence is checked, and step 2.1-2.4 are repeated in case it is not verified.

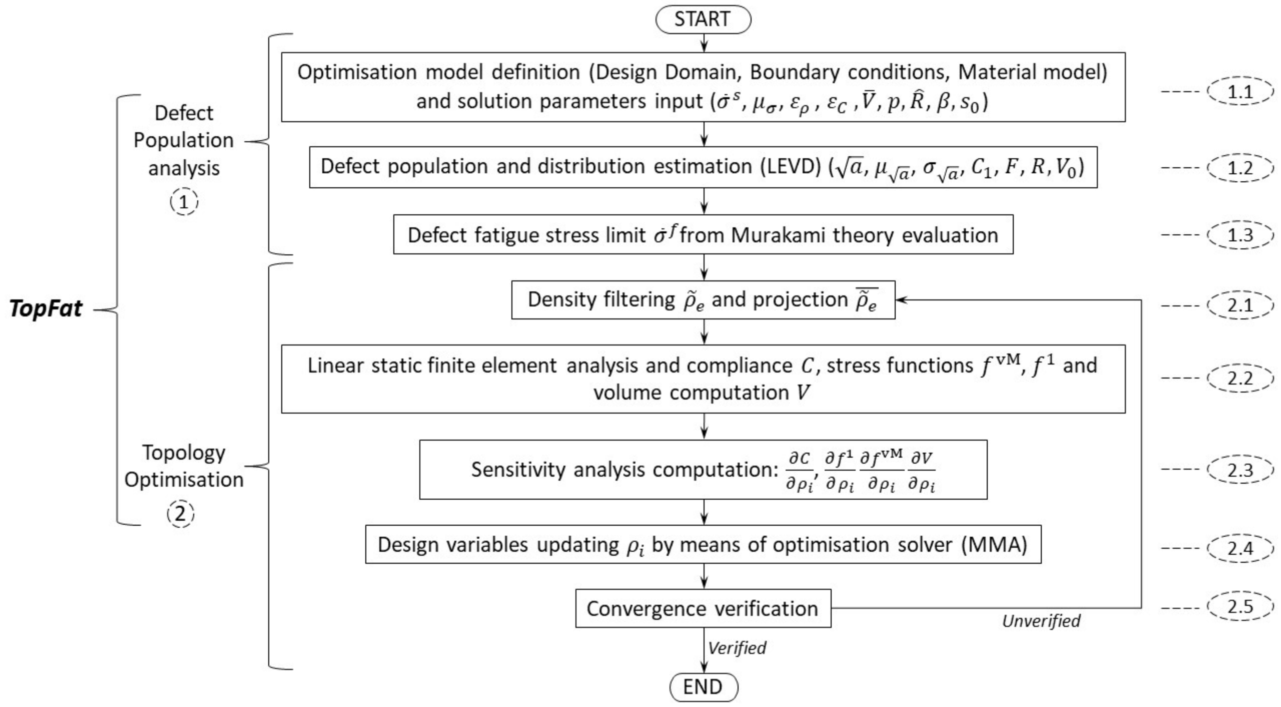

Figure 2 – Flowchart of the *TopFat* solution algorithm

4. Numerical examples

In this section, the proposed methodology is validated on literature benchmarks. In Sections 4.1, 4.2 and 4.3 the optimized topology of an L-shape structure, a cantilever and a corbel structure are assessed, respectively. For all the examples, steel is considered as constituent material, with Young's modulus $E = 2.1 \times 10^5$ MPa and Poisson's ratio $\nu = 0.3$, respectively. Initial designs with a uniform material distribution have been considered and all the initial values of the densities are set equal to 0.3. In Table 1 the values of the optimisation parameters are detailed.

SIMP parameter	**Value and/or continuation scheme**
Material interpolation p, Eq. (5)	$p = \min\{1 + \text{floor}((I-1)/3) \cdot 0.1, 3\}$
Stress aggregation measure μ_σ ,Eqs. (12) & (13)	$\mu_\sigma = 10$
Relaxation parameter s_0, Eqs. (16) &(17)	$s_0 = 0.618$
Linear filter radius $\hat{R}$, Eqs. (19) & (20), [39]	$\hat{R}/l_e = \max\{R_0 - \text{floor}((I-1)/10) \cdot 0.1, R_{min}\}$ $R_0 = 4; R_{min} = 1.2$

Nonlinear projection β, Eq. (21)	$\beta = \begin{cases} 0.1 & if\ I < 400 \\ \min\{0.1 + \mathrm{floor}((I/10 - 40)), 20\} & if\ I \geq 400 \end{cases}$
Convergence tolerance parameters ε_C , ε_ρ, Eq. (22)	$\varepsilon_C = 0.01$; ε_ρ =0.01

Table 1 – Values of optimisation parameters

Note: I is the iteration index, floor *is the function getting the highest integer less than or equal to the argument, l_e is the length of the side of the element e, R_{min} and R_0 are the minimum filter radius and the initial one.*

Table 2 lists the parameters related to the defect distribution and fatigue strength [30]. C_1 has been set conservatively to 1.41 (worst condition in [30]). A Vickers hardness of $290\ \mathrm{HV}$, consistent with the employed material, has been considered. The stress ratio R is set equal to 0. The volume V_n for each case is conservatively set equal to $\bar{V}$, the volume of the final topology, supposing that all the elements could contain the most critical defect. The reference volume for the LEVD is equal to $8.8 \times 10^{-3}\ \mathrm{mm}^3$, which is reasonably the inspection volume for defect sampling on the metallographic polished sample with an inspection area of about $0.5\ \mathrm{mm}^2$ [30]. The probability P has been set to 0.5 (i.e., the median quantile of the defect size in the final volume was considered). It is worth to note that a more conservative quantile can be chosen. However, since other conservative assumptions were made for the validation benchmarks (i.e., fatigue limit for surface defects and the presence of the critical defect in each element), the choice of the median quantile was considered appropriate. In addition, reasonable values from the literature have been considered or have been assumed, in order to show the effectiveness of the proposed methodology and the need of taking into account the material sensitivity to defect in the topology optimisation process.

Fatigue parameter	**Value**
Defect location parameters C_1	$C_1 = 1.41$
Vickers hardness HV	$HV = 290$
LEVD location parameter $\mu_{\sqrt{a}}$ $[\mu m]$	$\mu_{\sqrt{a}} = 16.96$
LEVD scale location parameter $\sigma_{\sqrt{a}}[\mu m]$	$\sigma_{\sqrt{a}} = 2.389$
Probability P	$P = 0.5$
Stress ratio R	$R = 0$
Reference volume $V_0[mm^3]$	$V_0 = 8.8 \cdot 10^{-3}$
Initial volume V_s $[mm^3]$	$V_s^{L-shape} = 6400$
	$V_s^{cantilever} = 20000$
	$V_s^{corbel} = 17700$
Upper limit volume, $\bar{V}$	$\bar{V} = 0.3 \cdot V_s$

Table 2 – Values of defect and fatigue parameters

4.1 L-shape structure design

In the first example, the optimized material distribution within a classical L-shape structure, shown in Fig. 3, is assessed. This domain geometry has been fairly employed in the literature and it is largely used for testing the effectiveness of stress-constrained TO algorithms [48][15]. The material volume is constrained to 30% of the design domain volume (i.e., $\bar{V} = 0.3 \cdot \bar{V}_{\mathrm{L-shape}}$). The design domain is discretized into 6400 square four-node elements with the edge length $1\,\mathrm{mm}$. To avoid the artificial stress concentration, the concentrated load $F = 800\,N$ is distributed equally over the closest five nodes around the vertical-right corner. The fatigue strength of the material, computed according to Eq. (4) by considering a volume corresponding to $0.3 \cdot \bar{V}_{\mathrm{L-shape}}$, leads to a limit of the first principal alternate stress of $\bar{\sigma}^f = 255\ \mathrm{MPa}$. For the von Mises stress constraint, an admissible stress $\bar{\sigma}^s = 580\ \mathrm{MPa}$ is considered (e.g., yield strength divided by an opportune safety coefficient).

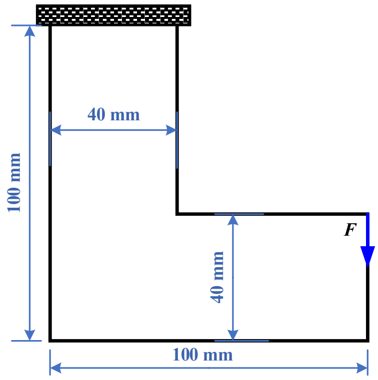

Figure 3 - L-shape design domain and geometrical dimensions.

The optimized topologies of the L-shape domain are obtained by considering four different constraint conditions (Fig. 4). Fig. 4a shows the optimized topology with only the volume constraint, Fig. 4b shows the optimized topology with the volume and the von Mises constraint, Fig. 4c shows the optimized topology with the volume and the fatigue constraint on the first principal alternate stress and Fig. 4d shows the optimized topology with all the constraints. In the figure, C is the compliance, $\sigma_{\max}^{\mathrm{vM}}$ is the maximum von Mises stress, $\sigma_{max}^1 = \max\limits_e(\sigma_e^1)$ is the maximum first principal alternate stress within the final domain.

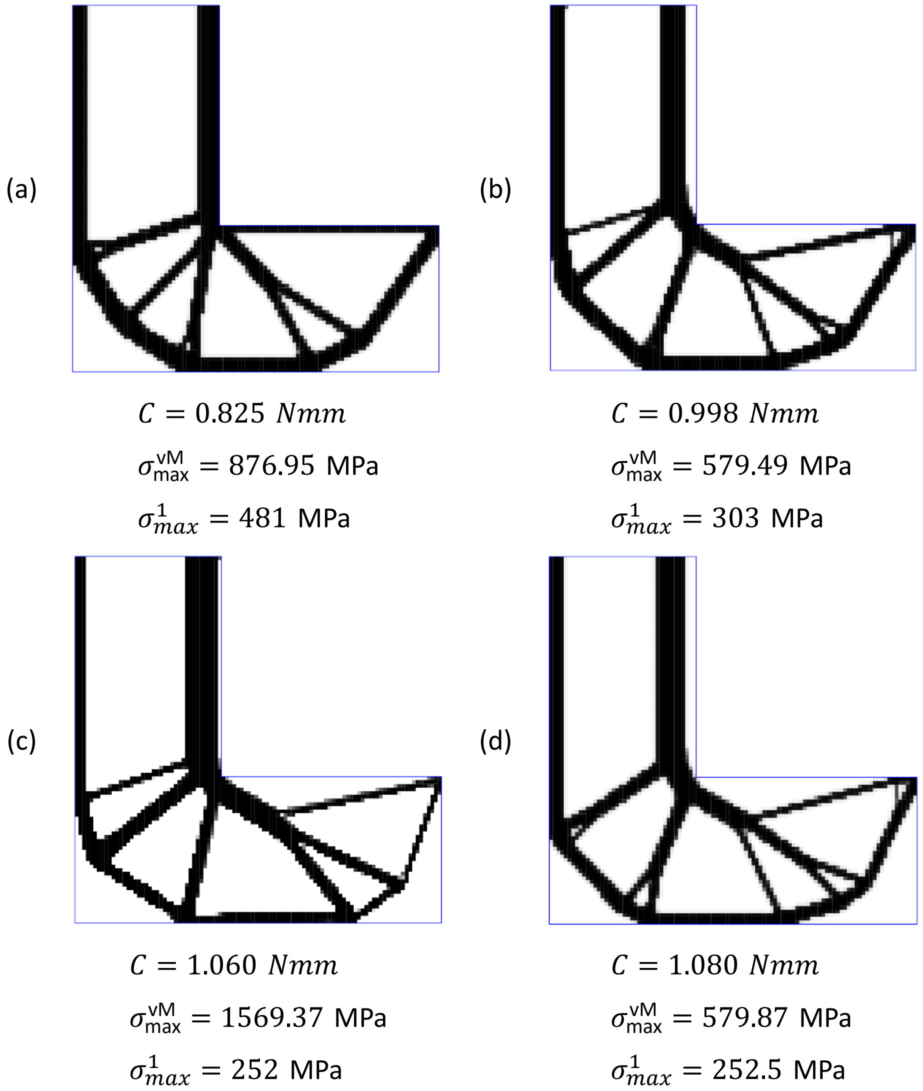

(a)

$C = 0.825\ Nmm$

$\sigma_{\text{max}}^{\text{vM}} = 876.95$ MPa

$\sigma_{max}^{1} = 481$ MPa

(b)

$C = 0.998\ Nmm$

$\sigma_{\text{max}}^{\text{vM}} = 579.49$ MPa

$\sigma_{max}^{1} = 303$ MPa

(c)

$C = 1.060\ Nmm$

$\sigma_{\text{max}}^{\text{vM}} = 1569.37$ MPa

$\sigma_{max}^{1} = 252$ MPa

(d)

$C = 1.080\ Nmm$

$\sigma_{\text{max}}^{\text{vM}} = 579.87$ MPa

$\sigma_{max}^{1} = 252.5$ MPa

Figure 4 - Optimisation results for the L-shape structure under different constraints. (a) only volume constraint; (b) volume and von Mises stress constraint (no fatigue constraint); (c) volume and fatigue constraint (no von Mises constraint); (d) volume and both stress and fatigue constraints.

As shown in Fig. 4 the solution to the classical compliance minimization problem under volume constraint (Fig. 4a) provides the minimum compliance compared to the other topologies. This represents the topology with the highest stiffness (C is the smallest), but both the von Mises stress and the first principal alternate stress are significantly larger than the material limits, compromising the structural integrity. Indeed, the re-entrant corner is still present in the design obtained, even if it is the most critical part of the entire domain since it is characterised by high and detrimental stress peaks. If the von Mises stress constraint is added (Fig. 4b), the final topology changes and the corner is smoothed, with the von Mises stress below the limit but the first principal alternate stress above the fatigue strength. The compliance, on the contrary, increases by about 20%. The topology in Fig. 4c, obtained by considering the constraints on the first principal alternate stress (fatigue constraint) and on the volume, is quite similar to the one showed in Fig. 4b. However, the members close to the corner are thicker, and thinner far from it, ensuring a first principal alternate stress below the prescribed fatigue strength, but with the von Mises stress significantly larger than the limit. In these three cases (Figs. 4 a-c), therefore, the structural integrity of the component is not guaranteed. Finally, Fig. 4d shows the topology of the fully constrained problem, i.e. under all the constraints on volume, von Mises and first principal alternate stress. It is useful to see these final topologies as an assembly of trusses. Indeed, the comparison of the thickness, location and orientation of these trusses in the final topologies can foster the understanding of their differences and peculiarities. The topology shown in Fig. 4d is qualitatively similar to those shown in Figs.4b and 4c, but the trusses dimensions are significantly different. In this case, both the maximum von Mises stress and the first principal alternate stress are below the limits, ensuring the structural integrity of the component. The compliance increment, about 29%, is compensated by a significant reduction in the stress level to completely satisfy the structural requirements, which is the most important aspect when a component is designed. Fig. 5 shows stress distributions in the topology obtained by considering all the constraints (Fig. 4d): Fig. 5a shows the first principal alternate stress, whereas Fig. 5b shows the von Mises stress.

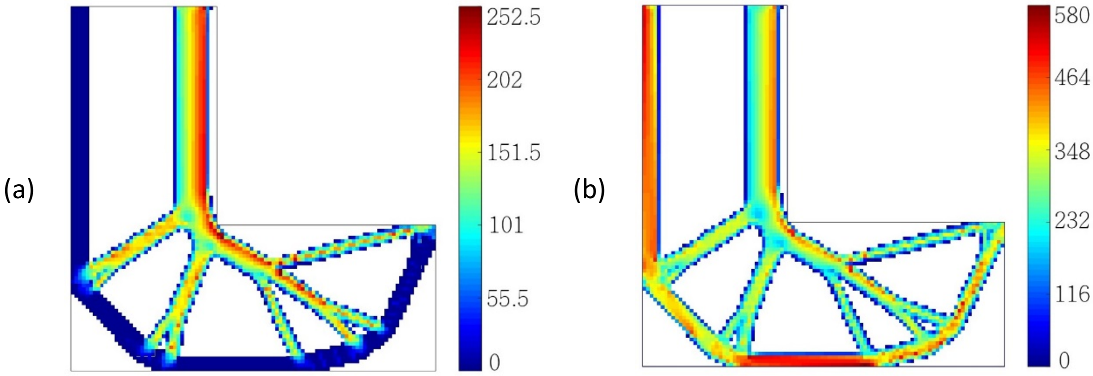

Figure 5 - Stress distribution of the optimized L-shape design under all types of constraints: (a) first principal alternate stress; (b) von-Mises stress

As shown in Fig. 5a, the first principal alternate stress in the lower trusses is close to 0 (blue colour), while it is close to the fatigue strength along the trusses close to the corner. For this reason, the lower trusses are thinner compared to the trusses close to the corner. The peak of the von Mises stress (Fig. 5b), on the contrary, is in the lower truss of the optimized domain. Fig. 5 confirms that both the stress constraints in the presented topology are respected.

Fig. 6a and Fig. 6b show the trend of the most meaningful quantities during the optimisation process. In particular, Fig. 6a shows the compliance and the stress with respect to the number of iterations (the compliance, the K-S fatigue function and the first principal alternate stress are shown); whereas Fig. 6b shows the material volume ratio and the stress with respect to the number of iterations (the K-S stress function and the maximum von Mises stress). As it can be noticed, the K-S aggregation function overestimates the real maximum in the structure. This is the reason why the STM-correction scheme is needed, as explained in Subsection 3.2.2. Overall, the combination of the aggregation function and the correction scheme reduces the number of constraints but guarantees that the real maximum value is set to the imposed limit.

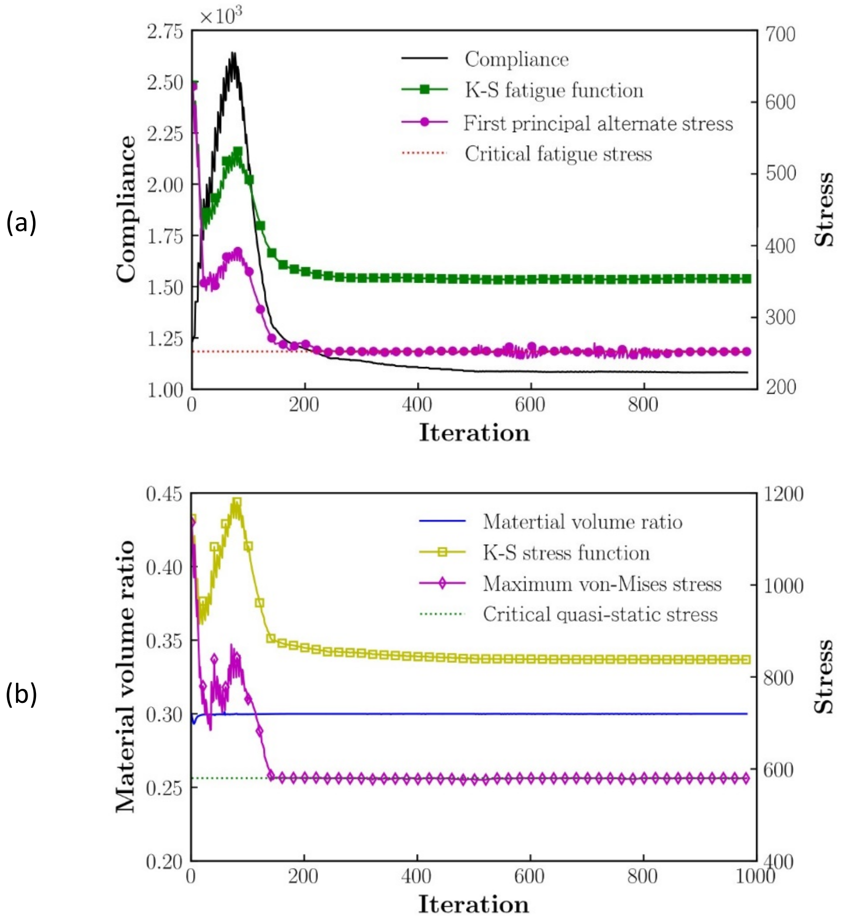

Figure 6 - Iteration histories for optimisation of the L-shape structure considering all types of constraints: (a) Compliance, K-S fatigue function and first principal alternate stress; (b) material volume ratio, K-S stress function and maximum von-Mises stress

As shown in Fig. 6a, the K-S fatigue function, the first principal alternate stress and the compliance share almost the same trend. A maximum appears around iteration number 100 and then these quantities rapidly decrease to their prescribed convergence values with few slight oscillations. The same considerations can be done for the von Mises stress and its K-S aggregation function (Fig. 6b). As for the volume ratio, it is almost constant during the process, mainly because the initial values of the design variables are set to the selected volume fraction, speeding up the convergence process of the volume constraint. Fig. 6 confirms therefore that the proposed algorithm rapidly converges to the prescribed values.

4.2 A cantilever structure design

A modified cantilever structure, shown in Fig. 7, is also considered for the validation of the proposed TO model and solution algorithm. As for the other examples, the prescribed material volume fraction is 0.30. The design domain is divided into 20,000 square four-node elements with of unit edge length. A concentrated load of $F = 1.0$ kN is distributed over thirteen neighbouring nodes along the right edge to avoid stress concentration. The fatigue strength $\bar{\sigma}^f$, computed according to Eq. (4), is equal to 253 MPa. As for the von Mises stress constraint, in this case it is set to $\bar{\sigma}^s = 620$ MPa.

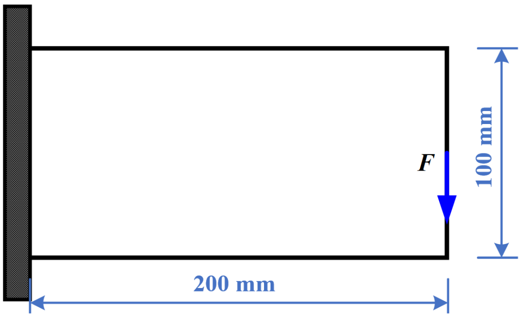

Figure 7 - Cantilever design domain and geometrical dimensions

As for the first example, four TOs with different constraints are carried out and the designs obtained are presented in Fig. 8. Fig. 8a shows the optimized topology with only the volume constraint, Fig. 8b shows the optimized topology with the volume and the von Mises stress constraints, Fig. 8c shows the optimized topology with the volume constraint and the fatigue constraint on the first principal alternate stress and Fig. 8d shows the optimized topology with all the constraints.

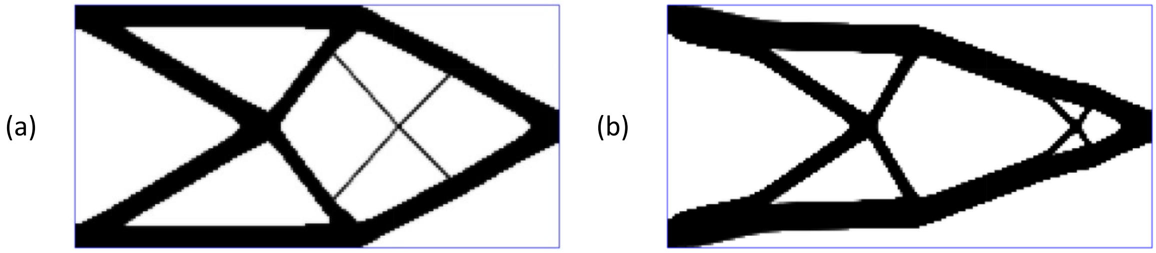

$C = 4.75$ Nmm

$\sigma^{\mathrm{vM}}_{\mathrm{max}} = 842.21$ MPa

$\sigma^{1}_{max} = 446$ MPa

$C = 5.16$ Nmm

$\sigma^{\mathrm{vM}}_{\mathrm{max}} = 619.93$ MPa

$\sigma^{1}_{max} = 328$ MPa

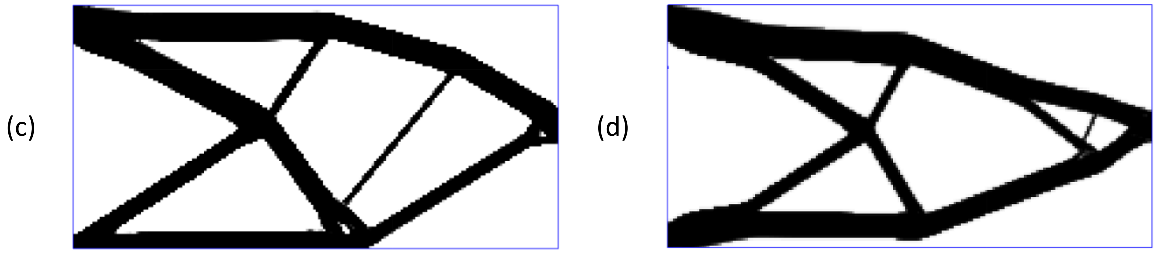

$C = 5.24\ N\text{mm}$ $C = 5.38\ N\text{mm}$

$\sigma_{\text{max}}^{\text{vM}} = 1054.05\ \text{MPa}$ $\sigma_{\text{max}}^{\text{vM}} = 620.00\ \text{MPa}$

$\sigma_{max}^{1} = 252\ \text{MPa}$ $\sigma_{max}^{1} = 252\ \text{MPa}$

Figure 8 - Optimisation results for the cantilever beam structure under different constraints. (a) only volume constraint; (b) volume and von Mises stress constraint (no fatigue constraint); (c) volume and fatigue constraint (no von Mises constraint); (d) volume and both stress and fatigue constraints.

According to Fig. 8, similar observations as for the L-shape structure can be made. The topology obtained by considering only the volume constraint is characterized by the maximum stiffness, but both the stresses (first principal alternate and von Mises) are larger than the admissible stresses. On the other hand, by considering only a limit on the von Mises stress (Fig. 8b) and a limit on the first principal alternate stress (Fig. 8c), one of the two stress constraints is violated. The fourth topology where both stress constraints are active (Fig. 8d) permits to respect both the material limits, with a compliance increment of about 13%, smaller than the increment in the L-shape structure.

Fig. 9 shows the stress distribution in the topology obtained by considering all the constraints (Fig. 8d): Fig. 9a shows the first principal alternate stress, whereas Fig. 9b shows the von Mises stress.

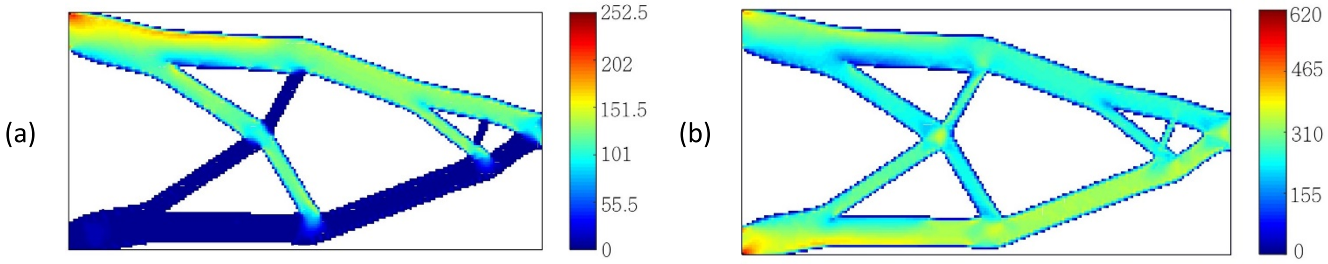

Figure 9 - Stress distribution of the optimized cantilever beam design under all types of constraints: (a) first principal alternate stress; (b) von-Mises stress.

By analysing Figs. 9a and 9b, the asymmetry induced by the fatigue constraint could be explained. Indeed, according to Figs. 8a and 8b, the final topology is vertically symmetric if constraints on the first principal alternate stress are not applied. On the contrary, the topologies in Figs. 8c and 8d, obtained by applying constraints on the first principal alternate stress, are not symmetric. Indeed, the von Mises stress is higher in the compressed trusses, whereas the first principal alternate stress prevails in the trusses subjected to traction, forcing them to be thicker and inducing a non-symmetric topology.

Figs. 10a and 10b show the trend of the most meaningful quantities during the optimisation process. In particular, Fig. 10a shows the compliance and the stress with respect to the number of iterations (the compliance, the K-S fatigue function and the first principal alternate stress are shown); whereas Fig. 10b shows the material volume ratio and the stress with respect to the number of iterations (the K-S stress function and the maximum von Mises stress).

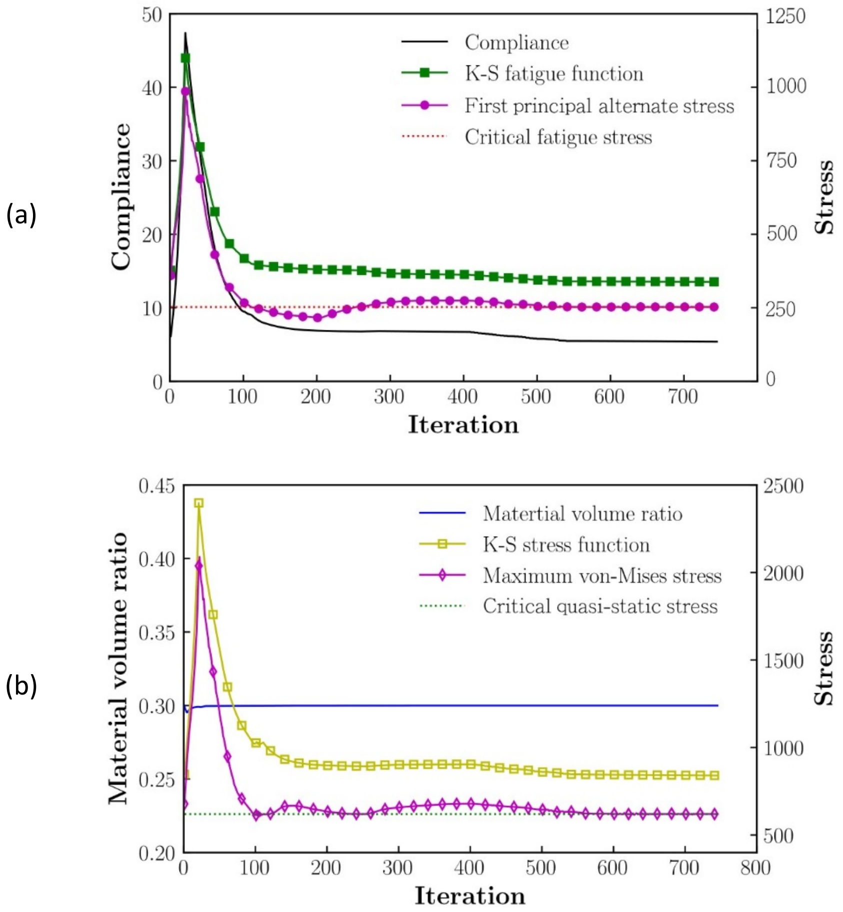

Figure 10 - Iteration histories for optimisation of the cantilever beam structure considering all types of constraints: (a) Compliance, K-S fatigue function and first principal alternate stress; (b) material volume ratio, K-S stress function and maximum von-Mises stress

The trends highlighted in Figs. 10a and 10b show that feasible designs are achieved in about 600 iterations and the convergence process is effective, with very little fluctuations. This means, as for the L-shape, that the proposed algorithm provides a smooth and clear method to find the optimal topology.

4.3 Corbel structure design

In the third example, a corbel structure [47] is considered (Fig. 11). The prescribed material volume fraction is 0.30. The design domain is meshed by 17700 square four-node elements of unit edge length. A concentrated load of $F = 3.5\ \mathrm{kN}$ is distributed over eleven neighbouring nodes along the top edge to avoid stress concentration. A fatigue strength $\bar{\sigma}^f$ of $253\ \mathrm{MPa}$ and a von Mises stress constraint $\bar{\sigma}^s$ of $660\ \mathrm{MPa}$ are considered.

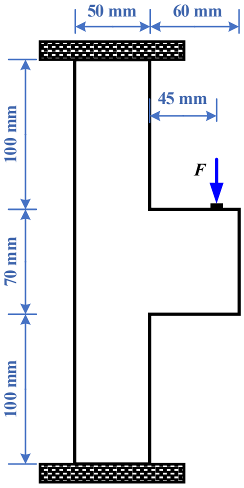

Figure 11 - Corbel design domain and geometrical dimensions

As for the other benchmarks, four cases are considered. Fig. 12a shows the optimized topology with only the volume constraint, Fig. 12b shows the optimized topology with the volume and the von Mises constraint, Fig. 12c shows the optimized topology with the volume and the fatigue constraint on the first principal alternate stress and Fig. 12d shows the optimized topology with all the constraints.

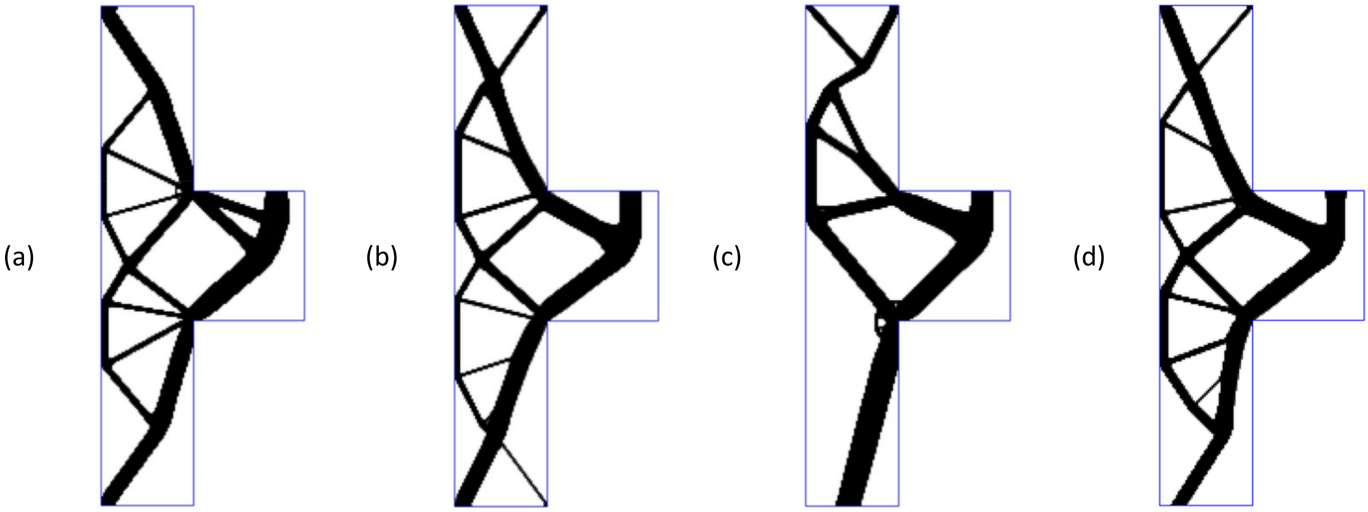

(a) $C = 16.96\ Nmm$ $\sigma_{\text{max}}^{\text{vM}} = 1309.00\ \text{MPa}$ $\sigma_{max}^{1} = 718\ \text{MPa}$

(b) $C = 19.79\ Nmm$ $\sigma_{\text{max}}^{\text{vM}} = 659.75\ \text{MPa}$ $\sigma_{max}^{1} = 333\ \text{MPa}$

(c) $C = 20.98\ Nmm$ $\sigma_{\text{max}}^{\text{vM}} = 1753.96\ \text{MPa}$ $\sigma_{max}^{1} = 252.5\ \text{MPa}$

(d) $C = 21.33\ Nmm$ $\sigma_{\text{max}}^{\text{vM}} = 659.01\ \text{MPa}$ $\sigma_{max}^{1} = 252.5\ \text{MPa}$

Figure 12 - Optimisation results for the corbel structure under different constraints. (a) only volume constraint; (b) volume and von Mises stress constraint (no fatigue constraint); (c) volume and fatigue constraint (no von Mises constraint); (d) volume and both stress and fatigue constraints.

This example further confirms the effectiveness of the proposed methodology. An increment of the compliance is compensated by the possibility to ensure the structural integrity of the optimized component. In the topology obtained by considering both constraints, the first principal alternate stress and the von

Mises stress are below the corresponding admissible values.

Fig. 13 shows the stress distribution in the topology obtained by considering all the constraints (Fig. 12d): Fig. 13a shows the first principal alternate stress, whereas Fig. 13b shows the von Mises stress.

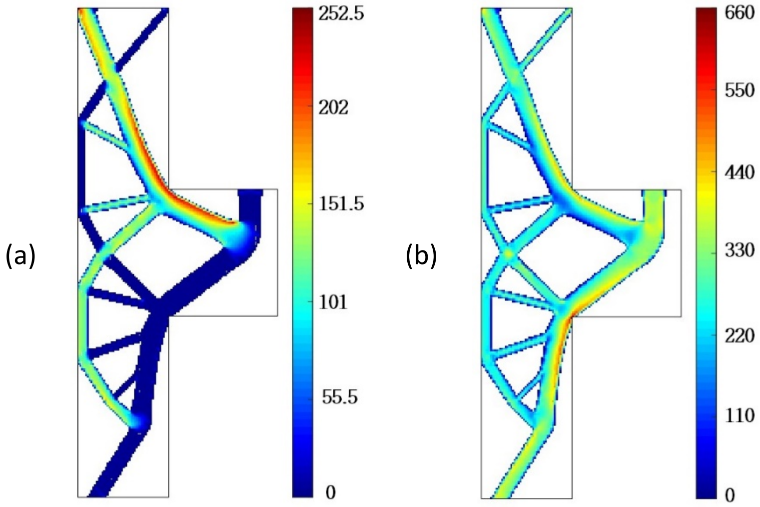

Figure 13 - Stress distribution of the optimized corbel design under all types of constraints: (a) first principal alternate stress; (b) von-Mises stress.

As for the other two cases, where the von Mises stress is higher, the first principal alternate stress is smaller and vice versa, highlighting the importance of considering both stress constraints.

Fig. 14a and Fig. 14b show the trend of the most meaningful quantities during the optimisation process. In particular, Fig. 14a shows the compliance and the stress with respect to the number of iterations (the compliance, the K-S fatigue function and the first principal alternate stress are shown); whereas Fig. 14b shows the material volume ratio and the stress with respect to the number of iterations (the K-S stress function and the maximum von Mises stress).

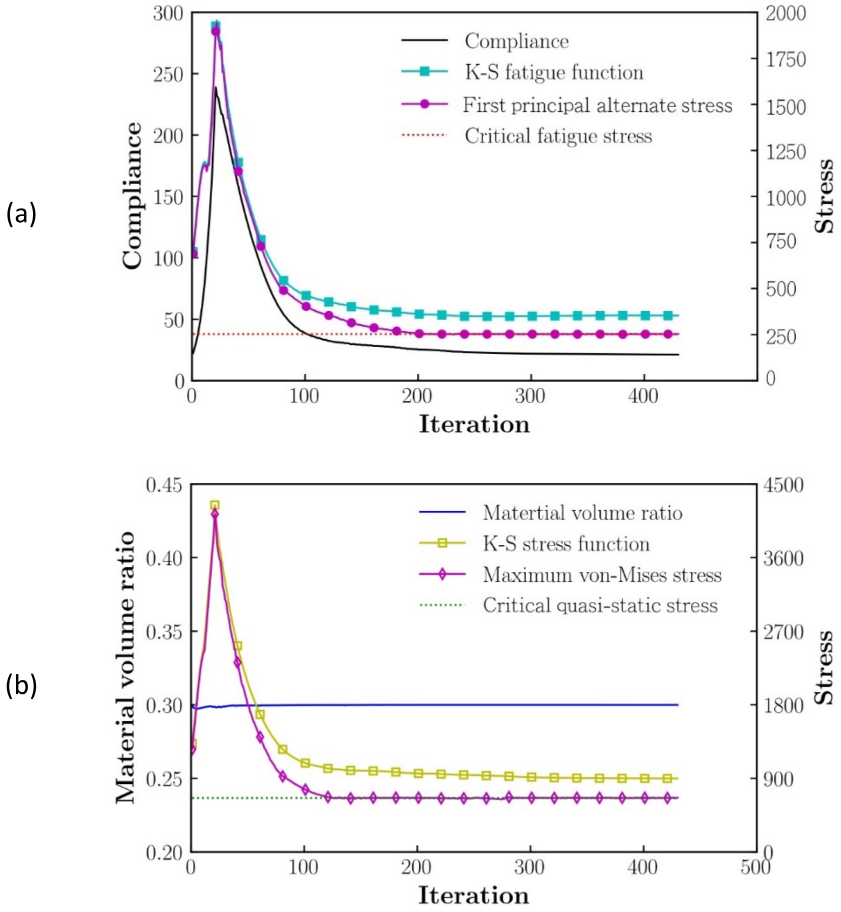

Figure 14 - Iteration histories for optimisation of the corbel structure considering all types of constraints: (a) Compliance, K-S fatigue function and first principal alternate stress; (b) material volume ratio, K-S stress function and maximum von-Mises stress

As for the other two examples, the algorithm rapidly converges (less than 200 iterations) with limited fluctuations, further proving the efficiency of the proposed TO algorithm with fatigue constraints.

Future works will be focused to fully consider more complex loading cases [57–60] by means of local approaches [61–63] also fully including three-dimensional effects [8,64–67].

5. Conclusions

In the present paper, a topology optimisation algorithm able to include the presence of defect as a fatigue limit is proposed. This defect-driven TO is able to provide safely optimised components and prevent from possible fatigue collapse in working conditions due to the presence of large defects which are generally neglected when components are designed. Indeed, material and manufacturing defects are the cause of fatigue failures in many components, especially in those produced through AM processes and generally designed with topology optimisation algorithms. In order to model the influence of defects on the fatigue response, a stress constraint on the first principal alternate stress is introduced in the topology optimisation algorithm. In particular, the first principal alternate stress, responsible for the crack nucleation and propagation from defects, is limited to a stress amplitude corresponding to the fatigue strength computed according to the well-known Murakami formulation. The dependency between the defect size and the material volume is also considered with the Largest Extreme Value Distribution (LEVD). A second stress constraint is introduced in order to limit the stress in elements subjected to compression stress and, therefore, not critical for the fatigue response. The proposed algorithm is validated with three literature benchmarks (L-shape, cantilever and corbel structures), evidencing its effectiveness.

The main results can be summarized as follows:

1. The proposed methodology provides a final topology with maximised stiffness under volume, quasi-static and fatigue constraints.
2. The fatigue constraint is defect driven, which is a fundamental aspect especially when designing components to be produced through Additive Manufacturing processes, characterized by a fatigue behaviour worse than that of components produced through traditional processes due to the presence of large manufacturing defects.
3. The main issues related to the density-based topology optimisation process and stress-constraints are considered and combined, guaranteeing smooth convergence.
4. The validation with three benchmarks confirms that the proposed algorithm permits to obtain a final topology with the first principal alternate stress below the fatigue strength in presence of defects and a von Mises stress below an admissible stress (e.g., yield stress divided by a safety coefficient) with a rapid convergence.

The proposed topology optimisation algorithm permits therefore to design fatigue resistant structures by taking manufacturing defects into consideration.

Appendix A: Hybrid stress element model definition

In this Appendix, the hybrid stress element model is formulated, and the related meaningful expressions are reported. The reader can refer to [40] for the full formulation and complete model analysis.

The expressions of the element vector stress and the displacement read:

$$\boldsymbol{\sigma}_e(\xi,\eta) = [\sigma_{ex} \quad \sigma_{ey} \quad \tau_{exy}]^T = \boldsymbol{\Phi}(\xi,\eta)\boldsymbol{\beta}_e \tag{A1}$$

$$\boldsymbol{u}_e(\xi,\eta) = [u_{ex} \quad u_{ey}]^T = \boldsymbol{N}(\xi,\eta)\boldsymbol{d}_e \tag{A2}$$

where σ_{ex}, σ_{ey} and τ_{exy} are the element stress components, u_{ex} and u_{ey} are the element displacement components, $\boldsymbol{\Phi}(\xi,\eta)$ and $\boldsymbol{N}(\xi,\eta)$ are the geometrical interpolation matrices depending on the element natural coordinates ξ and η for the stress and displacement respectively, $\boldsymbol{\beta}_e$ is the stress parameter vector and $\boldsymbol{d}_e$ is the element nodal displacement. As for the displacement field, the same interpolation scheme of bilinear quadrilateral four-node elements is used. As for the stress field, following [40] it is possible to express the stress parameter vector $\boldsymbol{\beta}_e$ as:

$$\boldsymbol{\beta}_e = \boldsymbol{H}^{-1}\boldsymbol{G}\boldsymbol{d}_e \tag{A3}$$

where the two matrices read:

$$\boldsymbol{G} = \int_{-1}^{1}\int_{-1}^{1} \boldsymbol{\Phi}^T\boldsymbol{B}\; t_0|\boldsymbol{J}|d\xi\; d\eta \tag{A4}$$

$$\boldsymbol{H} = \int_{-1}^{1}\int_{-1}^{1} \boldsymbol{\Phi}^T\boldsymbol{S}_0\boldsymbol{\Phi}\; t_0|\boldsymbol{J}|\; d\xi d\eta \tag{A5}$$

The terms reported in Eq. (A4) and Eq. (A5) are: $\boldsymbol{J}$ the Jacobian matrix and $|\boldsymbol{J}|$ its determinant, $\boldsymbol{B}$ the strain-displacement matrix, $\boldsymbol{S}_0$ the compliance matrix, i.e. the inverse of the elasticity matrix**,** and t_0 the structure thickness. Overall, the element stiffness matrix $\boldsymbol{k}_e$ and the element vector stress $\boldsymbol{\sigma}_e$ respectively read:

$$\boldsymbol{k}_e = \boldsymbol{G}^T\boldsymbol{H}^{-1}\boldsymbol{G} \tag{A6}$$

$$\boldsymbol{\sigma}_e = \boldsymbol{\Phi}\boldsymbol{H}^{-1}\boldsymbol{G}\boldsymbol{d}_e \tag{A7}$$

Thanks to Hellinger-Reissner variational principle [39,40] it is possible to find out the dependency with the density design variable ρ. The above described matrixes in the SIMP-TO framework read:

$$\boldsymbol{\beta}_e = \rho_e^{\gamma}\boldsymbol{H}^{-1}\boldsymbol{G}\boldsymbol{d}_e \tag{A8}$$

$$\boldsymbol{k}_e = \rho_e^{\gamma}\boldsymbol{G}^T\boldsymbol{H}^{-1}\boldsymbol{G} \tag{A9}$$

$$\boldsymbol{\sigma}_e = \rho_e^{\gamma}\boldsymbol{\Phi}\boldsymbol{H}^{-1}\boldsymbol{G}\boldsymbol{d}_e \tag{A10}$$

where the parameter γ is a scalar parameter defined by the employed interpolation technique.

Appendix B: Sensitivity Analysis

In this Appendix, the sensitivity analysis of the first principal alternate stress is detailed For the sensitivity of the compliance, the volume constraint and the von Mises constraint the reader is referred to Section 5 in [39].

The derivatives of the first principal alternate stress of the e^{th} element σ_e^1, defined in Eq. (10), with respect to the stress components $\sigma_{ex},\ \sigma_{ey},\ \tau_{exy}$, defined in Eq. (7), are given by:

$$\frac{\partial\sigma_e^1}{\partial\sigma_{ex}}=\frac{1}{2}+\frac{1}{2}\frac{\sigma_{ex}-\sigma_{ey}}{\sqrt{(\sigma_{ex}-\sigma_{ey})^2+4\tau_{exy}^2}}$$

$$\frac{\partial\sigma_e^1}{\partial\sigma_{ey}}=\frac{1}{2}-\frac{1}{2}\frac{\sigma_{ex}-\sigma_{ey}}{\sqrt{(\sigma_{ex}-\sigma_{ey})^2+4\tau_{exy}^2}} \tag{B1}$$

$$\frac{\partial\sigma_e^1}{\partial\tau_{exy}}=\frac{2\tau_{exy}}{\sqrt{(\sigma_{ex}-\sigma_{ey})^2+4\tau_{exy}^2}}$$

In matrix form the derivatives can be expressed as:

$$\frac{\partial\sigma_e^1}{\partial\boldsymbol{\sigma}_e}=\boldsymbol{V}_1^{\mathrm{T}}+\frac{1}{2}\frac{\boldsymbol{V}_2\boldsymbol{\sigma}_e}{(\boldsymbol{\sigma}_e^T\boldsymbol{V}_2\boldsymbol{\sigma}_e)^{\frac{1}{2}}} \tag{B2}$$

where $\boldsymbol{V}_1$ and $\boldsymbol{V}_2$ are detailed in Eq. (11).

The sensitivity of the K-S stress function in Eq. (13) with respect to ρ_i can be derived using the chain rule as:

$$\frac{\partial\sigma^{1,\mathrm{KS}}}{\partial\rho_i}=\sum_{e\in\Omega^1}\frac{\partial\sigma^{1,\mathrm{KS}}}{\partial\sigma_e^1}\left(\frac{\partial\sigma_e^1}{\partial\boldsymbol{\sigma}_{ce}}\right)^{\mathrm{T}}\frac{\partial\boldsymbol{\sigma}_{ce}}{\partial\rho_i} \tag{B3}$$

In the above expression, the partial derivative of the K-S stress function with respect to the element first principal alternate stress is detailed as below:

$$\frac{\partial\sigma^{1,\mathrm{KS}}}{\partial\sigma_e^1}=\frac{1}{\bar{\sigma}^f}\cdot\frac{exp\left(\mu_\sigma\frac{\sigma_e^1}{\bar{\sigma}^f}\right)}{\sum_{e\in\Omega^1}exp\left(\mu_\sigma\frac{\sigma_e^1}{\bar{\sigma}^f}\right)} \tag{B4}$$

The sensitivity of the element stress vector with respect to ρ_i is:

$$\frac{\partial\boldsymbol{\sigma}_{ce}}{\partial\rho_i}=\frac{q}{\rho_e}\delta_{ie}\boldsymbol{\sigma}_{ce}+\rho_e^q\boldsymbol{\Phi}_c\boldsymbol{H}^{-1}\boldsymbol{G}\frac{\partial\boldsymbol{d}_e}{\partial\rho_i} \tag{B5}$$

where δ_{ie} is the Kronecker delta. The adjoint method [15,50] is used to calculate the last term on the right-hand-side of Eq. (B5), which contains the sensitivity of the displacement vector. Following the same procedure as in [17] and after some rearrangements of the mathematical terms, it is possible to derive the expression for the sensitivity:

$$\frac{\partial \sigma^{1,\mathrm{KS}}}{\partial \rho_i} = \sum_{e\in\Omega^1} \frac{q\delta_{ie}}{\rho_e}\frac{\partial\sigma^{1,\mathrm{KS}}}{\partial\sigma_e^1}\left(\frac{\partial\sigma_e^1}{\partial\boldsymbol{\sigma}_{ce}}\right)^{\mathrm{T}}\boldsymbol{\sigma}_{ce} - \left(\boldsymbol{\chi}^{1,\mathrm{KS}}\right)^{\mathrm{T}}\frac{\partial\boldsymbol{K}}{\partial\rho_i}\boldsymbol{U} \tag{B6}$$

where $\boldsymbol{\chi}_k^{\mathrm{KS}}$ is an adjoint vector that can be obtained by solving the following:

$$\boldsymbol{K}\boldsymbol{\chi}_k^{\mathrm{KS}} = \sum_{e\in\Omega^1}\rho_e^q \frac{\partial\sigma_k^{\mathrm{KS}}}{\partial\sigma_e^1}\left(\boldsymbol{\Phi}_c\boldsymbol{H}^{-1}\boldsymbol{G}\right)^{\mathrm{T}}\frac{\partial\sigma_e^1}{\partial\boldsymbol{\sigma}_{ce}} \tag{B7}$$

The derivates of all the quantities can be achieved by the chain rule if the projected and filtered density is considered as reported in Section 6.1 in [39].

Acknowledgment

This work was supported by the National Natural Science Foundation of China [Grant No. 51808135] and Education Bureau of Guangdong Province [Grant No. 2017KQNCX061].

Declaration of competing Interest

The authors declared that there is no conflict of interest.

References

[1] Frazier WE. Metal additive manufacturing: A review. J Mater Eng Perform 2014;23:1917–28. https://doi.org/10.1007/s11665-014-0958-z.

[2] Lee H, Lim CHJ, Low MJ, Tham N, Murukeshan VM, Kim YJ. Lasers in additive manufacturing: A review. Int J Precis Eng Manuf - Green Technol 2017;4:307–22. https://doi.org/10.1007/s40684-017-0037-7.

[3] Yakout M, Elbestawi MA, Veldhuis SC. A review of metal additive manufacturing technologies. Solid State Phenom 2018;278 SSP:1–14. https://doi.org/10.4028/www.scientific.net/SSP.278.1.

[4] Gibson I, Rosen D, Stucker B. Additive Manufacturing Technologies. Springer; 2015.

[5] Hällgren S, Pejryd L, Ekengren J. (Re)Design for Additive Manufacturing. Procedia CIRP 2016;50:246–51. https://doi.org/10.1016/j.procir.2016.04.150.

[6] Plocher J, Panesar A. Review on design and structural optimisation in additive manufacturing: Towards next-generation lightweight structures. Mater Des 2019;183. https://doi.org/10.1016/j.matdes.2019.108164.

[7] Caivano R, Tridello A, Codegone M, Chiandussi G. A new methodology for thermostructural topology optimization: Analytical definition and validation. Proc Inst Mech Eng Part L J Mater Des Appl 2020. https://doi.org/10.1177/1464420720970246.

[8] Wu W, Hu W, Qian G, Liao H, Xu X, Berto F. Mechanical design and multifunctional applications of chiral mechanical metamaterials: A review. Mater Des 2019;180:107950. https://doi.org/10.1016/j.matdes.2019.107950.

[9] Liu J, Gaynor AT, Chen S, Kang Z, Suresh K, Takezawa A, et al. Current and future trends in topology optimization for additive manufacturing. Struct Multidiscip Optim 2018;57:2457–83. https://doi.org/10.1007/s00158-018-1994-3.

[10] Brusa E, Sesana R, Ossola E. Numerical modeling and testing of mechanical behavior of AM Titanium alloy bracket for aerospace applications. Procedia Struct Integr 2017;5:753–60. https://doi.org/10.1016/j.prostr.2017.07.166.

[11] Saadlaoui Y, Milan JL, Rossi JM, Chabrand P. Topology optimization and additive manufacturing: Comparison of conception methods using industrial codes. J Manuf Syst 2017;43:178–86. https://doi.org/10.1016/j.jmsy.2017.03.006.

[12] Caivano R, Tridello A, Paolino D, Chiandussi G. Topology and fibre orientation simultaneous optimisation: A design methodology for fibre-reinforced composite components. Proc Inst Mech Eng Part L J Mater Des Appl 2020;234:1267–79. https://doi.org/10.1177/1464420720934142.

[13] Bendsøe MP, Sigmund O. Topology Optimization: Theory, Methods and Applications. 2002.

[14] Sigmund O, Maute K. Topology optimization approaches: A comparative review. Struct Multidiscip Optim 2013;48:1031–55. https://doi.org/10.1007/s00158-013-0978-6.

[15] Holmberg E, Torstenfelt B, Klarbring A. Stress constrained topology optimization. Struct Multidiscip Optim 2013;48:33–47. https://doi.org/10.1007/s00158-012-0880-7.

[16] Gao X, Li L, Ma H. An Adaptive Continuation Method for Topology Optimization of Continuum Structures Considering Buckling Constraints. Int J Appl Mech 2017;9. https://doi.org/10.1142/S1758825117500922.

[17] Holmberg E, Torstenfelt B, Klarbring A. Fatigue constrained topology optimization. Struct Multidiscip Optim 2014;50:207–19. https://doi.org/10.1007/s00158-014-1054-6.

[18] Collet M, Bruggi M, Duysinx P. Topology optimization for minimum weight with compliance and simplified nominal stress constraints for fatigue resistance. Struct Multidiscip Optim 2017;55:839–55. https://doi.org/10.1007/s00158-016-1510-6.

[19] Oest J, Lund E. Topology optimization with finite-life fatigue constraints. Struct Multidiscip Optim 2017;56:1045–59. https://doi.org/10.1007/s00158-017-1701-9.

[20] Jeong SH, Lee JW, Yoon GH, Choi DH. Topology optimization considering the fatigue constraint of variable amplitude load based on the equivalent static load approach. Appl Math Model 2018;56:626–47. https://doi.org/10.1016/j.apm.2017.12.017.

[21] Nabaki K, Shen J, Huang X. Evolutionary topology optimization of continuum structures considering fatigue failure. Mater Des 2019;166:107586. https://doi.org/10.1016/j.matdes.2019.107586.

[22] Zhang S, Le C, Gain AL, Norato JA. Fatigue-based topology optimization with non-proportional loads. Comput Methods Appl Mech Eng 2019;345:805–25. https://doi.org/10.1016/j.cma.2018.11.015.

[23] Suresh S, Lindström SB, Thore CJ, Torstenfelt B, Klarbring A. Topology optimization using a continuous-time high-cycle fatigue model. Struct Multidiscip Optim 2020;61:1011–25. https://doi.org/10.1007/s00158-019-02400-w.

[24] Sherif K, Witteveen W, Puchner K, Irschik H. Efficient topology optimization of large dynamic finite element systems using fatigue. AIAA J 2010;48:1339–47. https://doi.org/10.2514/1.45196.

[25] Jeong SH, Choi DH, Yoon GH. Fatigue and static failure considerations using a topology optimization method. Appl Math Model 2015;39:1137–62. https://doi.org/10.1016/j.apm.2014.07.020.

[26] Lee JW, Yoon GH, Jeong SH. Topology optimization considering fatigue life in the frequency domain. Comput Math with Appl 2015;70:1852–77. https://doi.org/10.1016/j.camwa.2015.08.006.

[27] Zhao L, Xu B, Han Y, Xue J, Rong J. Structural topological optimization with dynamic fatigue constraints subject to dynamic random loads. Eng Struct 2020;205:110089. https://doi.org/10.1016/j.engstruct.2019.110089.

[28] Chen Z, Long K, Wen P, Nouman S. Fatigue-resistance topology optimization of continuum structure by penalizing the cumulative fatigue damage. Adv Eng Softw 2020;150:102924. https://doi.org/10.1016/j.advengsoft.2020.102924.

[29] Suresh S. Fatigue of Materials. Cambridge University Press; 1998. https://doi.org/10.1017/CBO9780511806575.

[30] Yukitaka Murakami. Metal Fatigue: Effects of Small Defects adn Nonmetallic Inclusions. Elsevier; 2002. https://doi.org/10.1016/B978-0-08-044064-4.X5000-2.

[31] Tang M, Pistorius PC. Oxides, porosity and fatigue performance of AlSi10Mg parts produced by selective laser melting. Int J Fatigue 2017;94:192–201. https://doi.org/10.1016/j.ijfatigue.2016.06.002.

[32] Yadollahi A, Shamsaei N. Additive manufacturing of fatigue resistant materials: Challenges and opportunities. Int J Fatigue 2017;98:14–31. https://doi.org/10.1016/j.ijfatigue.2017.01.001.

[33] Beretta S, Romano S. A comparison of fatigue strength sensitivity to defects for materials manufactured by AM or traditional processes. Int J Fatigue 2017;94:178–91. https://doi.org/10.1016/j.ijfatigue.2016.06.020.

[34] Tridello A, Fiocchi J, Biffi CA, Chiandussi G, Rossetto M, Tuissi A, et al. Effect of microstructure, residual stresses and building orientation on the fatigue response up to 109 cycles of an SLM AlSi10Mg alloy. Int J Fatigue 2020;137:105659. https://doi.org/10.1016/j.ijfatigue.2020.105659.

[35] Qian G, Li Y, Paolino DS, Tridello A, Berto F, Hong Y. Very-high-cycle fatigue behavior of Ti-6Al-4V manufactured by selective laser melting: Effect of build orientation. Int J Fatigue 2020;136:105628. https://doi.org/10.1016/j.ijfatigue.2020.105628.

[36] Martínez-Frutos J, Allaire G, Dapogny C, Periago F. Structural optimization under internal porosity constraints

using topological derivatives. Comput Methods Appl Mech Eng 2019;345:1–25. https://doi.org/10.1016/j.cma.2018.10.036.

[37] Tridello A, Fiocchi J, Biffi CA, Chiandussi G, Rossetto M, Tuissi A, et al. Influence of the annealing and defects on the VHCF behavior of an SLM AlSi10Mg alloy. Fatigue Fract Eng Mater Struct 2019;42:2794–807. https://doi.org/10.1111/ffe.13123.

[38] Bendsøe MP, Sigmund O. Material interpolation schemes in topology optimization. Arch Appl Mech (Ingenieur Arch 1999;69:635–54. https://doi.org/10.1007/s004190050248.

[39] Gao X, Li Y, Ma H, Chen G. Improving the overall performance of continuum structures: A topology optimization model considering stiffness, strength and stability. Comput Methods Appl Mech Eng 2020;359:1–23. https://doi.org/10.1016/j.cma.2019.112660.

[40] Pian THH, Sumihara K. Rational approach for assumed stress finite elements. Int J Numer Methods Eng 1984;20:1685–95. https://doi.org/10.1002/nme.1620200911.

[41] Patnaik SN, Guptill JD, Berke L. Singularity in structural optimization. Int J Numer Methods Eng 1993;36:931–44.

[42] Bruggi M. On an alternative approach to stress constraints relaxation in topology optimization. Struct Multidiscip Optim 2008;36:125–41. https://doi.org/10.1007/s00158-007-0203-6.

[43] Guo X, Cheng GD. S-relaxed approach in structural topology optimization. Struct Optim 1997:258–66.

[44] Le C, Norato J, Bruns T, Ha C, Tortorelli D. Stress-based topology optimization for continua. Struct Multidiscip Optim 2010;41:605–20. https://doi.org/10.1007/s00158-009-0440-y.

[45] Chen A, Cai K, Zhao ZL, Zhou Y, Xia L, Xie YM. Controlling the maximum first principal stress in topology optimization. Struct Multidiscip Optim 2020. https://doi.org/10.1007/s00158-020-02701-5.

[46] París J, Navarrina F, Colominas I, Casteleiro M. Topology optimization of continuum structures with local and global stress constraints. Struct Multidiscip Optim 2009;39:419–37. https://doi.org/10.1007/s00158-008-0336-2.

[47] Luo Y, Wang MY, Kang Z. An enhanced aggregation method for topology optimization with local stress constraints. Comput Methods Appl Mech Eng 2013;254:31–41. https://doi.org/10.1016/j.cma.2012.10.019.

[48] París J, Navarrina F, Colominas I, Casteleiro M. Block aggregation of stress constraints in topology optimization of structures. Adv Eng Softw 2010;41:433–41. https://doi.org/10.1016/j.advengsoft.2009.03.006.

[49] Kennedy GJ, Hicken JE. Improved constraint-aggregation methods. Comput Methods Appl Mech Eng 2015;289:332–54. https://doi.org/10.1016/j.cma.2015.02.017.

[50] Yang D, Liu H, Zhang W, Li S. Stress-constrained topology optimization based on maximum stress measures. Comput Struct 2018;198:23–39. https://doi.org/10.1016/j.compstruc.2018.01.008.

[51] Sigmund O, Petersson J. Numerical instabilities in topology optimization: A survey on procedures dealing with checkerboards, mesh-dependencies and local minima. Struct Optim 1998;16:68–75. https://doi.org/10.1007/BF01214002.

[52] Rozvany GIN. A critical review of established methods of structural topology optimization. Struct Multidiscip Optim 2009;37:217–37. https://doi.org/10.1007/s00158-007-0217-0.

[53] Bourdin B. Filters in topology optimization. Int J Numer Methods Eng 2001;50:2143–58. https://doi.org/10.1002/nme.116.

[54] Bruns TE, Tortorelli DA. Topology optimization of geometrically nonlinear structures and compliant mechanisms. 7th AIAA/USAF/NASA/ISSMO Symp Multidiscip Anal Optim 1998;190:1874–82. https://doi.org/10.2514/6.1998-4950.

[55] Wang F, Lazarov BS, Sigmund O. On projection methods, convergence and robust formulations in topology optimization. Struct Multidiscip Optim 2011;43:767–84. https://doi.org/10.1007/s00158-010-0602-y.

[56] Svanberg K. The method of moving asymptotes - a new method for structural optimization. Int J Numer Methods Eng 1987;24:359–73.

[57] Ayatollahi MR, Rashidi Moghaddam M, Razavi SMJ, Berto F. Geometry effects on fracture trajectory of PMMA samples under pure mode-I loading. Eng Fract Mech 2016;163:449–61. https://doi.org/10.1016/j.engfracmech.2016.05.014.

[58] Correia J, Apetre N, Arcari A, De Jesus A, Muñiz-Calvente M, Calçada R, et al. Generalized probabilistic model allowing for various fatigue damage variables. Int J Fatigue 2017;100:187–94. https://doi.org/10.1016/j.ijfatigue.2017.03.031.

[59] Berto F, Lazzarin P. Multiparametric full-field representations of the in-plane stress fields ahead of cracked components under mixed mode loading. Int J Fatigue 2013;46:16–26. https://doi.org/10.1016/j.ijfatigue.2011.12.004.

[60] Ferro P, Lazzarin P, Berto F. Fatigue properties of ductile cast iron containing chunky graphite. Mater Sci Eng A 2012;554:122–8. https://doi.org/10.1016/j.msea.2012.06.024.

[61] Torabi AR, Campagnolo A, Berto F. Local strain energy density to predict mode II brittle fracture in Brazilian disk

specimens weakened by V-notches with end holes. Mater Des 2015;69:22–9. https://doi.org/10.1016/j.matdes.2014.12.037.

[62] Berto F, Gallo P, Lazzarin P. High temperature fatigue tests of un-notched and notched specimens made of 40CrMoV13.9 steel. Mater Des 2014;63:609–19. https://doi.org/10.1016/j.matdes.2014.06.048.

[63] Zhu SP, Yu ZY, Correia J, De Jesus A, Berto F. Evaluation and comparison of critical plane criteria for multiaxial fatigue analysis of ductile and brittle materials. Int J Fatigue 2018;112:279–88. https://doi.org/10.1016/j.ijfatigue.2018.03.028.

[64] Berto F, Lazzarin P, Kotousov A. On higher order terms and out-of-plane singular mode. Mech Mater 2011;43:332–41. https://doi.org/10.1016/j.mechmat.2011.03.004.

[65] Berto F, Lazzarin P, Wang CH. Three-dimensional linear elastic distributions of stress and strain energy density ahead of V-shaped notches in plates of arbitrary thickness. Int J Fract 2004;127:265–82. https://doi.org/10.1023/B:FRAC.0000036846.23180.4d.

[66] Pook LP, Campagnolo A, Berto F. Coupled fracture modes of discs and plates under anti-plane loading and a disc under in-plane shear loading. Fatigue Fract Eng Mater Struct 2016;39:924–38. https://doi.org/10.1111/ffe.12389.

[67] Benedetti M, du Plessis A, Ritchie RO, Dallago M, Razavi SMJ, Berto F. Architected cellular materials: A review on their mechanical properties towards fatigue-tolerant design and fabrication. Mater Sci Eng R Reports 2021;144:100606. https://doi.org/10.1016/j.mser.2021.100606.